ChemSusChem

Research Article
doi.org/10.1002/cssc.202202281

Chemistry Europe
European Chemical Societies Publishing

www.chemsuschem.org

Investigation of SnS_2-rGO Sandwich Structures as Negative Electrode for Sodium-Ion and Potassium-Ion Batteries

Chengping Li,[a, b, c] Kristina Pfeifer,[b] Xianlin Luo,[b] Georgian Melinte,[d] Jinsong Wang,[a] Zhengfu Zhang,*[a] Yingjie Zhang,[c] Peng Dong,[c] Angelina Sarapulova,[b] Helmut Ehrenberg,[b] and Sonia Dsoke*[b]

Sodium-ion and potassium-ion batteries (NIBs and KIBs) are considered promising alternatives to replace lithium-ion batteries (LIBs) in energy storage applications due to the natural abundance and low cost of Na and K. Nevertheless, a critical challenge is that the large size of Na^+/K^+ leads to a huge volume change of the hosting material during electrochemical cycling, resulting in rapid capacity decay. Among negative candidates for alkali-metal-ion batteries, SnS_2 is attractive due to the competitively high specific capacity, low redox potential and high abundance. Porous few-layer SnS_2 nanosheets are in situ grown on reduced graphene oxide, forming a SnS_2-rGO sandwich structure via strong C–O–Sn bonds. This nano-scaled sandwich structure not only shortens Na^+/K^+ and electron transport pathways but also accommodates volume expansion, thereby enabling high and stable electrochemical cycling performance of SnS_2-rGO. This work explores the influence of different conductive carbons (Super P and C65) on the SnS_2-rGO electrode. In addition, the effects of the electrolyte additive fluoroethylene carbonate (FEC) on the electrochemical performance in NIBs and KIBs is evaluated. This work provides guidelines for optimized electrode structure design, electrolyte additives and carbon additives for the realization of better NIBs and KIBs.

Introduction

The rapidly increasing demands for lithium-ion batteries (LIBs) are faced with low abundance and uneven geographical distribution of lithium.[1–3] Sodium-ion batteries (NIBs) and potassium-ion batteries (KIBs) are considered promising alternatives to LIBs due to their similar storage mechanism, the higher abundance of sodium and potassium, low cost of raw materials and the possibility of using the cost-effective Al current collector at both electrodes.[4–14] In addition, the redox standard hydrogen potential of Na^+/Na (−2.71 V vs. standard hydrogen electrode [SHE]) is higher than that of Li^+/Li (−3.05 V vs. SHE) and the redox standard K^+/K (−2.93 V vs. SHE) is close to that of Li^+/Li.[15,16] However, the radius of the K ions (1.38 Å) and Na ions (1.02 Å) are larger than that of Li ions (0.76 Å), which would cause serious structure rebuilding and sluggish kinetics for Na^+/K^+ transfer during the electrochemical process, leading to inferior structure stability and fast capacity decay.[15,17,18] At present, carbon-based materials only show rather low reversible capacities. Graphite shows a specific capacity of $\approx$279 mAh g^{-1} (corresponding to KC_8) in KIBs, while Na^+ does not intercalate into graphite under the common conditions applied in NIBs, delivering a very low specific capacity (35 mAh g^{-1}, NaC_{64}).[19] Hard carbons are the most used negative electrodes in NIBs and KIBs due to rich pores and large interlayer spacing.[1] However, these carbon-based negative materials cannot meet the increasing demands for NIBs and KIBs. On the other hand, conversion and alloying type materials can provide much higher specific capacity and they are therefore subjects of intensive research.

Sn-based compounds like Sn_4P_3,[20,21] or SnS_2,[22,23] operating via conversion and alloying reactions in Na^+/K^+ storage, are considered as some the most promising negative electrode candidates due to their high theoretical capacity of 1136 mAh g^{-1}.[24] Among them, SnS_2 with a layered CdI_2 crystalline-like structure ($a=b=3.65$ Å, space group $\bar{P}m1$) consists of Sn atoms sandwiched between two hexagonal layers of S atoms. The interlayer space ($c=5.90$ Å) is higher than the one of graphite (3.4 Å) and can promote fast ionic diffusion.[25–27] However, SnS_2-based negative electrodes suffer from the inherently poor electrical conductivity and structure degrada-

[a] Dr. C. Li, Dr. J. Wang, Prof. Dr. Z. Zhang
Faculty of Materials Science and Engineering
Kunming University of Science and Technology
Kunming 650093 (P. R. China)
E-mail: zhang-zhengfu@kust.edu.cn
[b] Dr. C. Li, Dr. K. Pfeifer, Dr. X. Luo, Dr. A. Sarapulova, Prof. Dr. H. Ehrenberg, Dr. S. Dsoke
Institute for Applied Materials (IAM)
Karlsruhe Institute of Technology (KIT)
Hermann-von-Helmholtz-Platz 1, 76344 Eggenstein-Leopoldshafen (Germany)
E-mail: sonia.dsoke@kit.edu
[c] Dr. C. Li, Prof. Dr. Y. Zhang, Prof. Dr. P. Dong
National and Local Joint Engineering Laboratory for Lithium-ion Batteries and Materials Preparation Technology
Kunming University of Science and Technology
Kunming 650093 (P. R. China)
[d] Dr. G. Melinte
Institute of Nanotechnology (INT)
Karlsruhe Institute of Technology (KIT)
Hermann-von-Helmholtz-Platz 1, 76344 Eggenstein-Leopoldshafen (Germany)

Supporting information for this article is available on the WWW under https://doi.org/10.1002/cssc.202202281

tion caused by huge volume expansion during repeated Na^+/K^+ insertion/de-insertion processes, subsequently leading to pulverization of the active material and losing electrical contact with the Al current collector.

There are some useful strategies to tackle this challenge, including the control of the particle size and the dispersion of the nanoparticles by incorporation in a conductive matrix. For example, Bin et al.[28] reported that SnS_2/graphene electrodes can deliver a reversible capacity of 610 mAh g^{-1} at 50 mA g^{-1} and a high rate capability of around 290 mAh g^{-1} at 2 A g^{-1}. Li et al.[17] prepared SnS_2@C@rGO electrodes with a reversible capacities up to 721 mAh g^{-1} at 50 mA g^{-1} and 298 mAh g^{-1} at 500 mA g^{-1} in NIBs and KIBs, respectively. Reduced graphene oxide (rGO) has beneficial features like a large surface area, excellent conductivity, and good flexibility, and it was therefore considered an outstanding matrix for loading layered materials. However, in previously reported research works,[29–32] the assembly between SnS_2 nanoparticles and rGO was mostly suffering from poor physical interconnection. Therefore, the interfacial bonding between active particles and carbon matrices was not very intimate and effective, leading to electrode degradation during cycling. On the other hand, it is highly desirable to develop controllable and reliable strategies for fabricating novel nanostructured SnS_2/carbon matrix composites.

A composite of porous few-layer SnS_2 nanosheets in situ grown on rGO is proposed: A SnS_2/rGO/SnS_2 sandwich structure, which is expected to possess both high capacity and excellent cycling operation. In this SnS_2/rGO/SnS_2 sandwich structure, SnS_2 nanosheets are closely anchored on the surface of rGO sheets via a strong C–O–Sn bond. The designed structure is featured with: 1) few-layer SnS_2 nanosheets, which shorten the Na^+/K^+ diffusion pathway and facilitate the kinetics of Na^+/K^+ movement. The porous structure alleviates mechanical strain caused by repeated volume change due to sodium/potassium-ion insertion/extraction processes; 2) rGO layers, which provide pathways with high electron conductivity and a flexible cushion layer to buffer the anisotropic volumetric expansion. Therefore, the unique SnS_2/rGO sandwich structure is endowed with high electrochemical activity. The function of electrolyte additives such as fluoroethylene carbonate (FEC) on Na^+/K^+ storage performance will be investigated.

FEC has been demonstrated as a promising electrolyte additive for NIBs, capable of improving reversible capability and retention stabilities. Komaba et al.[33] found that FEC can improve passivation, suppression of side reactions and the reversibility for hard-carbon and $NaNi_{1/2}Mn_{1/2}O_2$ electrodes. Bie et al.[34] also checked the function of the FEC additive in KIBs and found that FEC caused inferior cyclic performance of graphite electrode. However, the understanding of FEC on electrolytes based on Na salts and K salts is insufficient and needs in-depth investigations. Therefore, the SnS_2-rGO electrode was chosen as model system to investigate the effects of FEC on structural stability, cycling performance and SEI components.

Results and Discussion

Structure and morphology of SnS_2-rGO

The crystal structure and phase ratios of SnS_2-rGO were investigated by X-ray diffraction (XRD) as shown in Figure 1a. The Rietveld refinement shows that the SnS_2-rGO product contains SnS_2 ($P\bar{3}m1$, 63%) and rGO ($Fmmm$, 37%). In this composite, the cell parameters of SnS_2 are $a=b=3.621$ Å, $c=6.443$ Å, and the cell parameters of rGO are $a=2.464$ Å, $b=4.154$ Å, $c=6.271$ Å. XPS measurements are conducted to investigate the chemical components and oxidation states of Sn and S in the composite. In the Sn 3d spectrum two peaks located at 487.2 and 495.6 eV are related to Sn $3d_{5/2}$ and Sn $3d_{3/2}$, which confirms the presence of Sn^{4+} in SnS_2.[22,32] The additional two small peaks at 488.0 and 496.4 eV correspond to Sn $3d_{5/2}$ and Sn $3d_{3/2}$ of Sn^{4+} in SnO_2 (Figure 1b). This is due to SnS_2 contact with O_2 forming SnO_2 on the surface. The spectrum of the S 2p is divided into two kinds of doublets (Figure 1c). The first doublet consists of the peaks located at 162.1 eV (S $2p_{3/2}$) and 163.3 eV (S $2p_{1/2}$) related to the binding energies of SnS_2.[35] The second doublet is composed of the peaks at 164.0 eV (S $2p_{3/2}$) and 165.1 eV (S $2p_{1/2}$), which correspond to the formation of C–S–C, indicating that S is might have covalent bonds with carbon.[22,36,37] The spectra of C 1 s are assigned to four signals (Figure 1d): 285.0 eV for C–C/C=C, 286.0 eV for C–O–C, 287.0 eV for C–S and 289.1 eV for O–C=O.[38,39] These results further support that SnS_2-rGO composites have been successfully prepared.

The porous SnS_2-rGO sandwich was prepared by using a sacrificed microcubic $MnCO_3$ template. The microcubic $MnCO_3$ can provide many pores, which shorten Na^+/K^+ transport and buffer volume expansion during electrochemical reactions. Rietveld refinement demonstrates that the $MnCO_3$ template crystallizes with space group $R\bar{3}c$ and cell parameters $a=b=4.795$ Å and $c=15.692$ Å (Figure S1a). The controlled self-assembly of $MnCO_3$ shows a microcube structure with an average size of 2–3 μm (Figure S1c in the Supporting Information). The intermediate product $MnCO_3$@SnS_2-rGO (Figure S1d) sample shows a typical nanosheet structure. $MnCO_3$ microcubes in the $MnCO_3$@SnS_2-rGO product are observed. The $MnCO_3$ template was removed by hydrochloric acid treatment to obtain a porous structure. It will be checked if vacancies develop surrounding the SnS_2 nanosheets and if they are beneficial for facilitating the electrolyte impregnation and counteracting volume variations during repeated electrochemical cycling. Additionally, the Raman spectra of the porous SnS_2-rGO are given in Figure S1b. The peak at 311.7 cm^{-1} is related to the A_{1g} Raman-active vibration mode. The rGO is characterized by the disordered D band and graphitic G bands at 1330 and 1590 cm^{-1}, which are assigned to the defects in the hexagonal graphitic layer and the vibration of carbon atoms in a 2D hexagonal lattice, respectively.[40–42] The intensity ratio of I_D/I_G is 1.17, which indicates that the rGO has a highly disordered carbon structure compared with the well-ordered graphite ($I_D/I_G<0.5$).

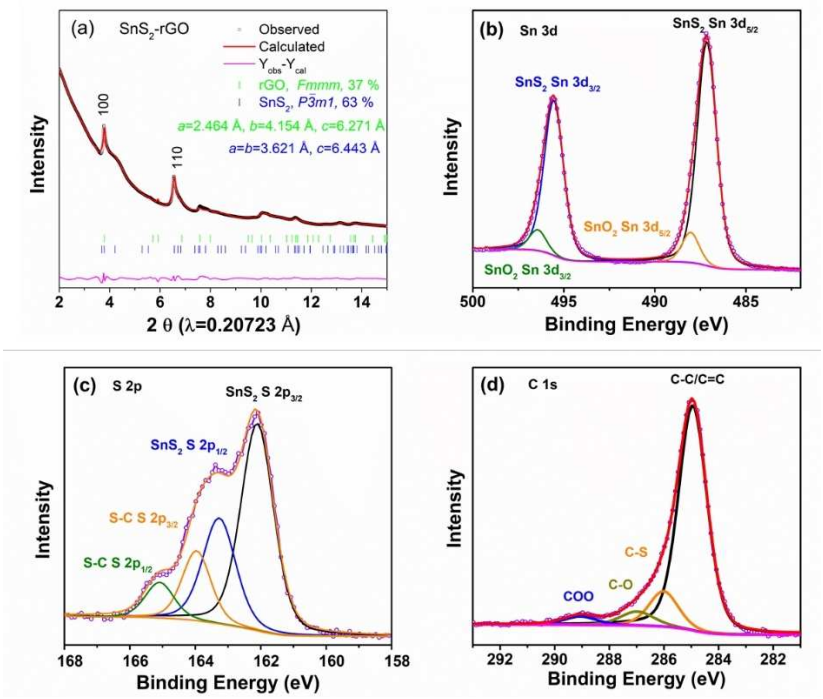

Figure 1. Rietveld refinement based on X-ray radiation diffraction data of SnS_2-rGO (a), high-resolution XPS spectra Sn 3d (b), S 2p (c), and C 1 s (d) of SnS_2-rGO.

The prepared SnS_2-rGO has wrinkled sheet-like morphology (Figure 2a). The high magnification SEM image (Figure 2b) shows that SnS_2 has nanocrystals with an average size of 2–4 nm and reveals few-layered features. The EDX mappings show that the SnS_2-rGO is composed of Sn (Figure S2b), S (Figure S2c), and C (Figure S2d). The Sn, S and C signals are homogeneous, implying a uniform chemical composition distribution and high structure affinity between the rGO sheets and the SnS_2 nanosheets. The carbon percentage of the SnS_2-rGO composite is 15.6%, which was obtained from Organic Elemental Analysis (OEA, Table S1). The TEM image further demonstrates the ultrafine SnS_2 nanocrystals (Figure 2c). Thermogravimetric analysis (TGA) was performed to determine the carbon content in the SnS_2-rGO composite and shown in Figure S3. The mass loss of the SnS_2-rGO composite undergoes three steps. The initial mass loss (3.4%) ranging from 30 to 250 °C is due to the evaporation of physically absorbed water. In the second step, from 250 to 500 °C, the weight loss (24.8%) is associated with the oxidation of SnS_2 into SnO_2. The third weight loss step (500–800 °C) (15.6%) is owing to the decomposition of rGO into CO_2 and H_2O. The carbon percentage obtained from TGA is consistent with the OEA result. The selected area electron diffraction (SAED) in the inset of Figure 2c displays a series of diffraction rings with interlayer distances of 0.310, 0.210, and 0.180 nm, corresponding to the (100), (102), and (110) planes of crystalline SnS_2.[22,27] The HR-TEM image of the edge (Figure 2d) shows SnS_2 nanosheets lying between rGO nanosheets, confirming that SnS_2 nanosheets are in situ grown on the rGO nanosheets. The lattice spacing of 0.61 nm is consistent with the (001) crystalline planes of SnS_2.[43] The diffraction ring 100 with an interlayer distance of 0.310 nm is obtained from the fast Fourier transform (FFT) of HR-TEM data. The amorphous rGO marked by the arrow can be easily observed. The energy-filtered transmission electron microscopy (EFTEM) and EDX elemental mapping images (Figure 2e) and the high-resolution elemental and chemical maps using electron energy loss spectroscopy (EELS) (Figure S4) further demonstrate that SnS_2 nanosheets are homogeneously distributed in rGO. Based on the above-mentioned surface morphology analysis, it is concluded that SnS_2 nanosheets are not only in situ grown on the rGO nanosheets but also surrounded by carbon. The unique structure is composed of ultrasmall SnS_2 nanosheets and a highly conductive rGO nanosheets network, which can shorten sodium/potassium-ions diffusion pathways and tolerate volume expansion. Therefore, high performance of the SnS_2-rGO electrode for NIBs and KIBs is expected.

Characterization of Na^+ storage performance

As shown in Figure 3a, the SnS_2-rGO electrode in the FEC-free electrolyte can deliver a capacity of 270 mAh g^{-1} after 300 cycles, whereas the SnS_2-rGO electrode in the 5 wt% FEC-containing electrolyte can maintain an almost constant capacity of 417 mAh g^{-1} over 300 cycles. It is found that the coulombic efficiency (CE) values with FEC are lower than without FEC, implying there are parasitic side reactions for all 300 cycles with FEC. As a consequence a thicker SEI film should have formed and more Na^+ consumed for the 5 wt% FEC-containing electrolyte. This is verified by the high intensity of the XPS peak from

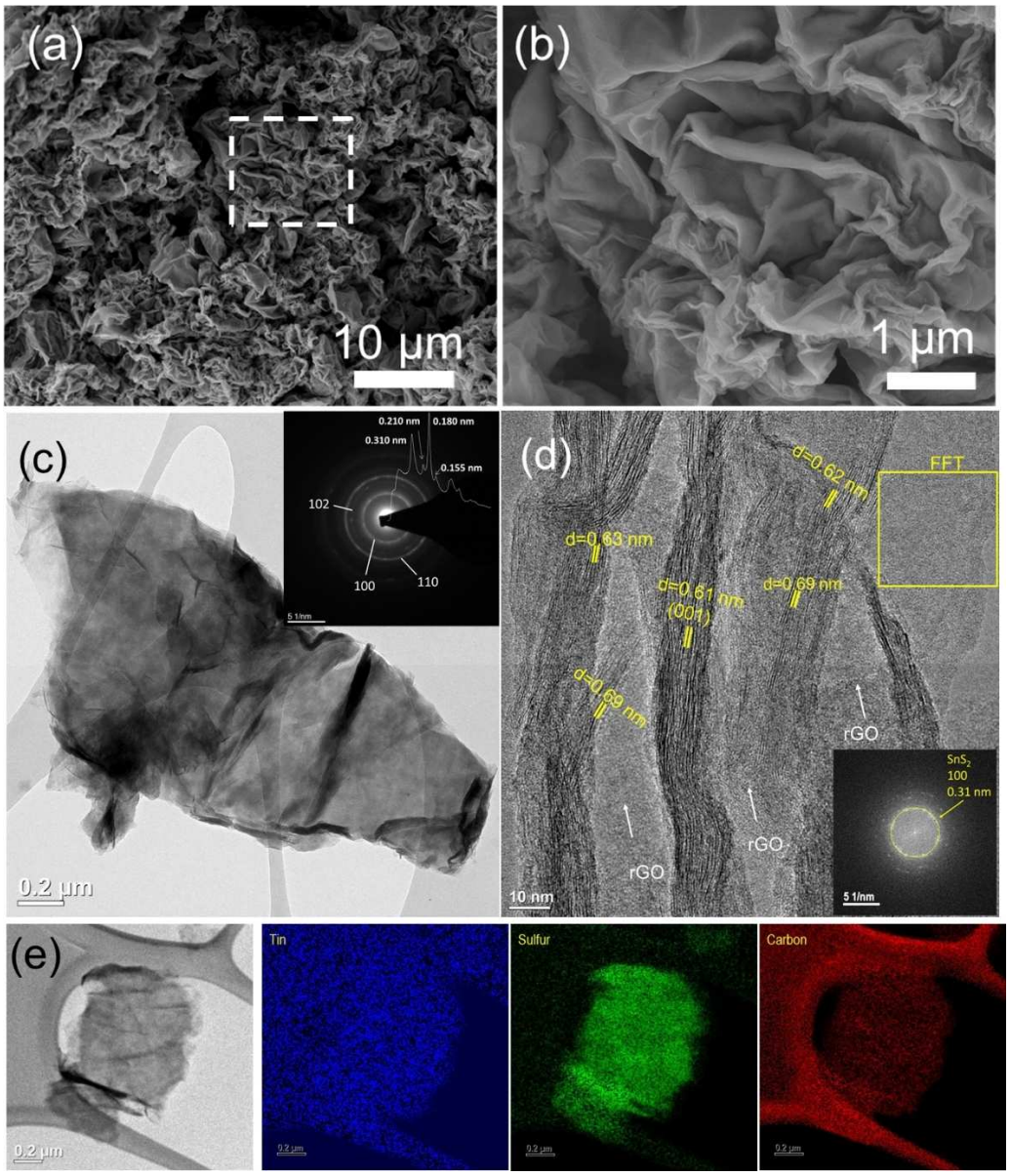

Figure 2. SEM image (a), high-magnification SEM image (b), TEM image (c) (inset: diffraction rings of SAED pattern), HR-TEM image (d), EFTEM image (e), and Sn, S and C elemental mapping images of SnS_2-rGO.

the sample after 20 cycles at electron energies, corresponding to Na–F bonds (Figure 3c). Therefore, the formation of such a thicker SEI layer consumed more Na-ions during the reduction process and resulted in lower capacities. Figure 3b compares the specific capacities of the SnS_2-rGO electrodes after the 1st, 2nd and 300th cycles with 5 wt% FEC-containing and FEC-free electrolytes, respectively. However, the SnS_2-rGO electrode exhibits superior cycling stability in the 5 wt% FEC-containing electrolytes. The presence of FEC can improve the cycle performance of the electrode material, similar to what was obtained by Komaba et al.[33] with $NaNi_{1/2}Mn_{1/2}O_2$ electrodes in aprotic Na half-cells. 1 M $NaClO_4$ in ethylene carbonate/dimethyl carbonate (EC/DMC = 1 : 1) with 5 wt% FEC was therefore selected as the main electrolyte for further experiments. XPS measurements were performed to investigate the chemical valence and components of SEI formed on the SnS_2-rGO electrode surface after 20 cycles, as shown in Figure 3c–d. In the F 1 s spectra (Figure 3c), F–O (687.1 eV) and Na–F (683.9 eV) bonds are emerging in the 5 wt% FEC-containing electrolyte and FEC-free electrolyte, while the intensities of F–O (687.1 eV) and Na–F (683.9 eV) bonds in the 5 wt% FEC-containing electrolyte are higher than that without FEC, indicating that FEC is beneficial for stable SEI formation. As shown in Figure 3d (C 1 s spectra), compared with the fresh SnS_2-rGO electrode, new C–C (283.6 eV) and CO_3 (290.0 eV) bonds are observed, which can be attributed to the decomposition and reduction of EC, DMC and FEC. In the Sn 3d spectra (Figure S5a), the weak peak of Sn $3d_{5/2}$ located at 486.5 eV is observed in the fresh

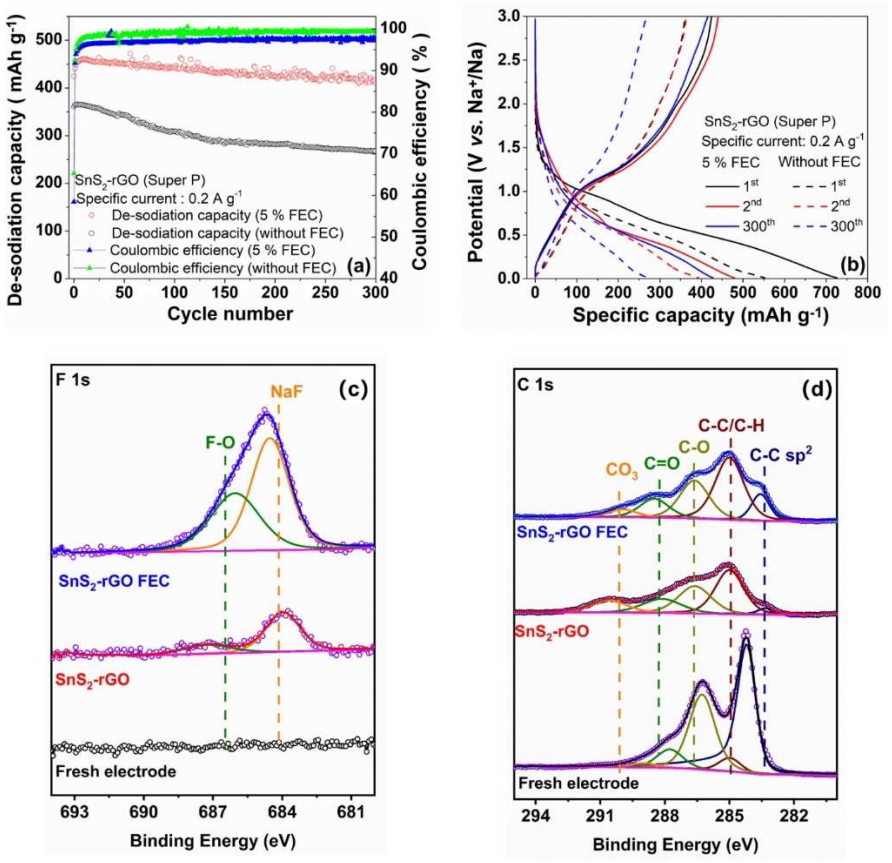

Figure 3. (a) Long-term cycling stability of the SnS_2-rGO electrode in the 5 wt% FEC-containing electrolyte and FEC-free electrolyte; and (b) the specific capacity of the SnS_2-rGO electrode in the 1st, 2nd and 300th cycles, respectively; (c) F 1 s and (d) C 1 s XPS of the SnS_2-rGO electrodes after 20 cycles.

SnS_2-rGO electrode, while this peak disappears in the cycled electrodes, which confirms the formation of an SEI layer, which absorbs the corresponding photoelectrons. The broadening of the S 2p spectra in Figure S5b, which is due to the conversion and alloying reactions, leads to sodium polysulfides Na_2S_x ($2 < x < 8$) formation.[44]

SEM characterization was used to observe the surface morphology of the SnS_2-rGO electrodes after 20 cycles in the 5 wt% FEC-containing electrolyte and FEC-free electrolyte. The SnS_2-rGO electrode in the FEC-free electrolyte exhibits some cracks on the surface (Figure S5c), and a thicker SEI layer is observed on the surface (Figure S5d). The SEI film is damaged /repaired repeatedly upon cycling, causing continuous depletion of the electrolyte, particle pulverization and loss of electric contact with the Al current collector. In contrast, in the 5 wt% FEC-containing electrolyte, fewer cracks emerge on the surface (Figure S5e), and the enlarged surface shows a porous structure (Figure S5f). With FEC additive, FEC first reduces to form Na_2CO_3 and fluorine-rich organic compounds, forming a polymeric stable and thin SEI film on the surface of the material, which can better tolerate the volume expansion of the SnS_2-rGO electrode.[45] These factors contribute to the superior properties of the SnS_2-rGO electrode in FEC-based electrolytes. The EDS elemental mapping of the SnS_2-rGO (Super P) electrode after 20 cycles in the FEC-free electrolyte and in the 5 wt% FEC-containing electrolyte are shown in Figure S6a and b, respectively. The images indicate uniform distributions of Sn, S, C, and Na, in the sodiated product, and a homogenous distribution of Sn and S in the desodiated product.

Study on the Na^+ storage mechanism in SnS_2-rGO electrode

To study the Na^+ storage mechanism of SnS_2-rGO electrodes, cyclic voltammetry (CV) measurements were performed with a scan rate of 0.05 mV s^{-1} in a voltage range of 0.01–3.0 V vs. Na^+ /Na, shown in Figure 4a and b. Due to the inherently low conductivity of SnS_2, carbon additives are crucial for the percolation and electrochemical activity of SnS_2-based negative electrodes. However, understanding the properties and the effect of different carbon additives in SnS_2-based electrodes is still lacking so far. In this work, we investigated the Na^+ storage performance in SnS_2-rGO electrodes with different carbon additives (namely Super P and C65). According to previous works, Super P and C65 have different Na and K self-storage capacities; therefore, we chose them for comparison.[46] During the first sodiation process, three clear cathodic peaks are visible at 1.88, 1.04, and 0.47 V. The small shoulder at 1.88 V could be associated with Na^+-ions insertion between SnS_2 layers forming Na_xSnS_2 [Eq. (1)].[27,47] The peak at 1.04 V is attributed to the

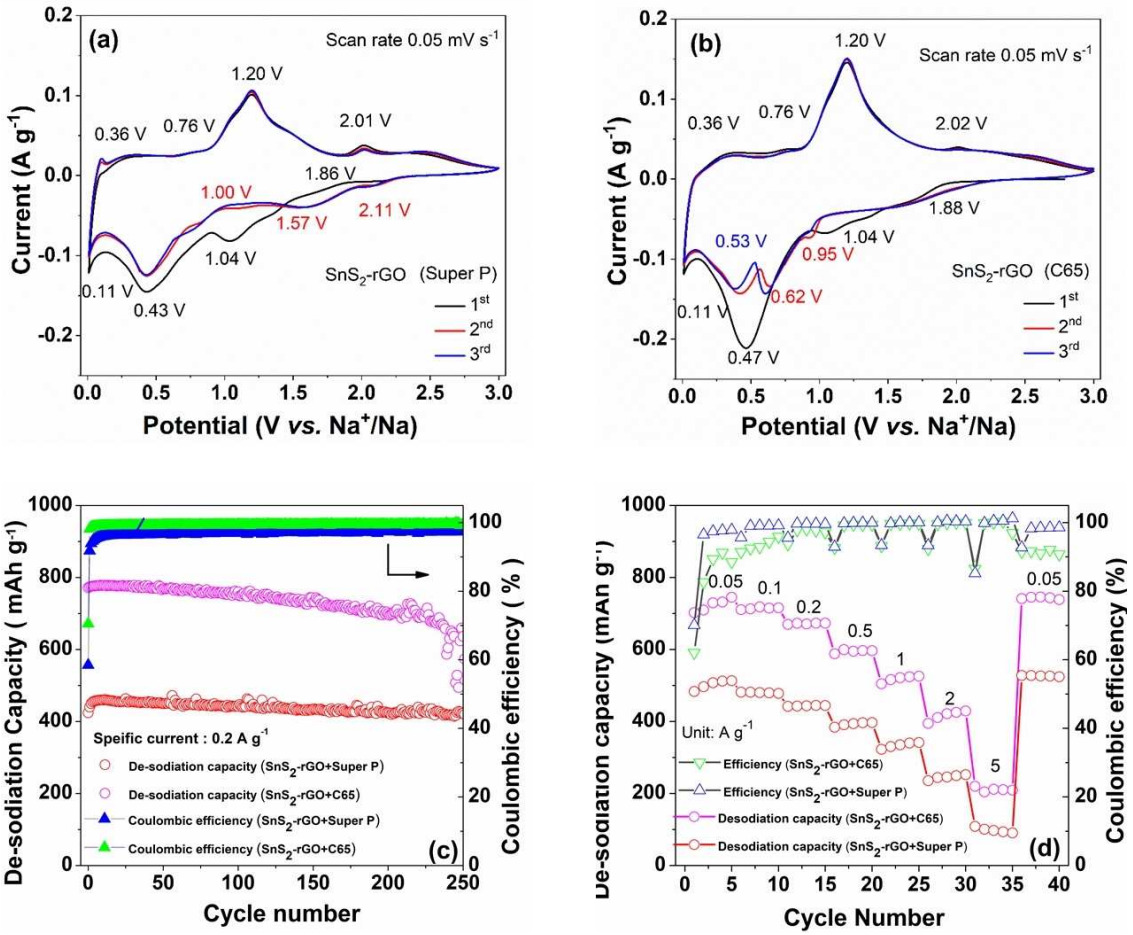

Figure 4. CV curves of the SnS_2-rGO electrode at a scan rate of 0.05 mV s^{-1} in the voltage range of 0.01–3.0 V vs. Na^+/Na with different carbon additives: Super P (a) and C65 (b). Electrochemical performances of the SnS_2-rGO electrode: The long-term cycling and CE with Super P and C65 conductive carbons at a specific current of 0.2 A g^{-1} (c); rate performance (d).

conversion of Na_xSnS_2 into metallic Sn and the formation of Na_2S [Eq. (2)]. The other cathodic peak at 0.47 V can be ascribed to the Na–Sn alloying process [Eq. (3)] and the formation of a solid–electrolyte interphase (SEI).[25,43] The corresponding oxidation peaks can be observed in the following anodic scan. The oxidation peak at 0.36 V is due to the de-alloying of $Na_{3.75}Sn$.[48] The peak at 0.76 V can be assigned to the formation of Na_xSnS_2. The distinct oxidation peak at 1.20 V can be associated with the reformation of the SnS_2-rGO.[25] Furthermore, the 2nd and 3rd CV curves are well overlapping, indicating good electrochemical reversibility of the SnS_2-rGO composite during the sodiation and desodiation processes. However, the CV of the electrode prepared with Super P shows more redox peaks as compared with C65-containing electrode, which could be due to the storage ability of Super P and will be discussed later.

$$SnS_2 + x\,Na^+ + x\,e^- \rightleftharpoons Na_xSnS_2 \quad (1)$$

$$Na_xSnS_2 + (4-x)\,Na^+ + (4-x)\,e^- \rightleftharpoons Sn + 2\,Na_2S \quad (2)$$

$$Sn + 3.75\,Na^+ + 3.75\,e^- \rightleftharpoons Na_{3.75}Sn \quad (3)$$

Figure 4c depicts the long-term cycling performance of the SnS_2-rGO electrode with Super P and C65 carbon additives. The long-term electrochemical behavior was investigated at the specific current of 0.2 A g^{-1} in the potential window of 0.01–3.0 V vs. Na^+/Na. The SnS_2-rGO electrode with C65 exhibits excellent capacity retention during cycling. A reversible desodiation capacity of 635 mAh g^{-1} is retained after 250 cycles. In contrast, the SnS_2-rGO electrode with Super P delivers a reversible desodiation capacity of only 420 mAh g^{-1} after 250 cycles at the same specific current. However, the pure SnS_2 electrode shows reversible capacity of 90 mAh g^{-1} at the current density of 200 mA g^{-1},[49] therefore the SnS_2-rGO electrode exhibits superior electrochemical performance. Rate capability tests were performed at different specific currents from 0.05 to 5 A g^{-1} in the voltage range from 0.01 to 3.0 V vs. Na^+/Na for the SnS_2-rGO electrode and are shown in Figure 4d. The rate performance of the SnS_2-rGO electrode also proves the advantages of using C65. At the initial low current density of 0.05 A g^{-1}, a high reversible capacity of 720 mAh g^{-1} is delivered by the SnS_2-rGO electrode with C65. Upon increasing the current density to 0.1, 0.2, 0.5, 1, 2, and 5 A g^{-1}, the specific

capacity slightly decreases to 712, 675, 592, 522, 424, and 210 mAh g^{-1}, respectively. When the specific current is set back to 0.05 A g^{-1}, the specific capacity recovers to 745 mAh g^{-1}, which is even higher than the initial capacity of 720 mAh g^{-1}. In contrast, the specific capacity of the SnS_2-rGO electrode with Super P is much lower than that with C65 at all tested current densities. The Super P containing electrode delivers 513, 481, 442, 390, 339, and 207 mAh g^{-1} at specific currents of 0.05, 0.1, 0.2, 0.5, 1, 2, and 5 A g^{-1}, respectively. The apparently lower CE (blue triangles) in (Figure 4d) seem to be correlated with the changes of the currents. They are probably caused artefacts. It is important to notice that Super P and C65 are the most widely used conductive additives for LIBs and NIBs.[46,50,51] Both carbons have chain-like networks of round-shaped particles (20–30 nm).They display similar Brunauer–Emmett–Teller (BET) surface areas and pore volumes: Super P (62 m^2 g^{-1}, 0.11 cm^3 g^{-1}), C65 (64 m^2 g^{-1}, 0.12 cm^3 g^{-1}). Theoretically, the very similar chemical properties of Super P and C65 should not cause very different long-term cycling performance and rate performance. Pfeifer et al.[46] reported that the desodiation capacity of Super P and C65 is 170 mAh g^{-1} and 70 mAh g^{-1} at 0.2 A g^{-1}, respectively. This means that a component of Super P, which should be inactive, is active. The electrochemical activity of this conductive carbon could detrimentally influence the active material, leading to a loss of buffering features and causing the SnS_2-rGO electrode to crack. Also, the electronic conductive paths can be interrupted or destroyed if Super P itself expands. These considerations give some first and vague ideas about the differences between these two carbons and the lower capacity of the Super P-containing electrode.

Figure S7a and b present the sodiation/desodiation profiles of the SnS_2-rGO electrode with Super P and C65 conductive carbons of the 1st, 2nd, 3rd, 150th, and 250th cycle at a specific current of 0.2 A g^{-1}. In consistence with the CV curves, three plateaus and a sloping curve can be observed in the first sodiation process, associated with the formation of Na_xSnS_2 (1.88 V),[25] the conversion reaction (1.04 V), and alloying reaction (0.01–0.47 V), respectively.[47] Moreover, the first desodiation potential plateau at 1.22 V may appear due to the reformation of the original SnS_2 material.[26] The SnS_2-rGO electrode with Super P delivers a first sodiation capacity of 726 mAh g^{-1} and a desodiation capacity of 424 mAh g^{-1} with a CE of 58.5 %. The irreversible capacity loss of 302 mAh g^{-1} at the first cycle is attributed to the inevitable formation of the SEI film on the surface of the active material and electrolyte decomposition.[52] In contrast, the SnS_2-rGO electrode with C65 presents a first sodiation capacity of 1094 mAh g^{-1} and a desodiation capacity of 772 mAh g^{-1} with a CE of 70.5 %. Similarly, the irreversible capacity of 322 mAh g^{-1} at the first cycle takes place due to the formation of the SEI and electrolyte decomposition. The CE increases to 99 % after the second cycle and is maintained in the subsequent cycles, indicating the high reversibility of the electrochemical reactions. It is the unique SnS_2-rGO sandwich structures and the interaction between the SnS_2 nanocrystalline and rGO that result in the composite having a strong electrochemical rate performance and a high capacity. Figure S7c and d compare the specific capacity values of the SnS_2-rGO electrode with Super P and C65 conductive additives at various specific currents, respectively. The different long-term cycling and rate performance were inspiring to further investigate the kinetics and resistance parameters. Summary of the Sn-based sulfides electrodes materials for NIBs applications is shown in Table S2.

Study of the kinetic processes via multi-scan cyclic voltammetry and impedance spectroscopy

To further distinguish between surface-controlled and diffusion-controlled reactions of the SnS_2-rGO electrode, CV curves of the as-prepared SnS_2-rGO electrode at various scan rates ranging from 0.05 to 2 mV s^{-1} were recorded and shown in Figure 5. The CV curves exhibit the redox peaks at each scan rate, which matches well with the sodiation/desodiation profiles. Additionally, both current intensities of the SnS_2-rGO electrode with Super P (Figure 5a) and C65 (Figure 5b) increase with the increase of the scan rates. The CV curves maintain a similar shape even at the high scan rate of 2 mV s^{-1}. It's assumed that the current obeys a power-law with the scan rate [Eq. (4)].[53–55] In Equation (4), a and b are two adjustable parameters, v is the sweep rate and i is the peak current response. The value of b ranges from 0.5 to 1.0, where $b = 0.5$ indicates a diffusion (bulk)-controlled process, while $b = 1.0$ implies a surface-controlled process. One cathodic peak and one anodic peak are chosen to determine the relationship between log (i) and log (v) [Eq. (5)].[56–58] Figure 5c shows the linear fitting of log (i) and log (v). The values of b of the SnS_2-rGO electrode with Super P are 0.795 and 0.804 for the cathodic and anodic peaks, respectively. For the SnS_2-rGO electrode with C65, the b value for the cathodic and anodic peaks is 0.795 in both cases. The above-described analysis confirms that the surface-controls the electrochemical process in the SnS_2-rGO electrode during the initial cycles,[59] thus leading to high rate performance.

Furthermore, to quantify the surface contribution in the SnS_2-rGO electrode by using Equations (6) and (7). The current response (i) at a specific potential [V] can be divided into surface contribution (k_1v, named as Q_p) and diffusion (bulk)-controlled contribution ($k_2v^{0.5}$, named as Q_d). Figure 5d presents the relationship of $|\ i\ (v)|\ v^{-1/2}$ and $v^{1/2}$, and of the related coefficients k_1 and k_2. The surface contribution (Q_p) of the SnS_2-rGO electrode with Super P (Figure 5e) and C65 additive (Figure 5f) increases with the growth of the sweep rate, demonstrating that surface-controlled behavior holds competitive advantages in the whole electrochemical process, especially at high scan rates. Figure S8a and b display the detailed surface-controlled contribution at 1 mV s^{-1}.

$$i = av^b \tag{4}$$

$$\log|(i)| = b\log(v) + \log(a) \tag{5}$$

$$|i| = k_1v + k_2v^{0.5} \tag{6}$$

$$|i|v^{-0.5} = k_1v^{0.5} + k_2 \tag{7}$$

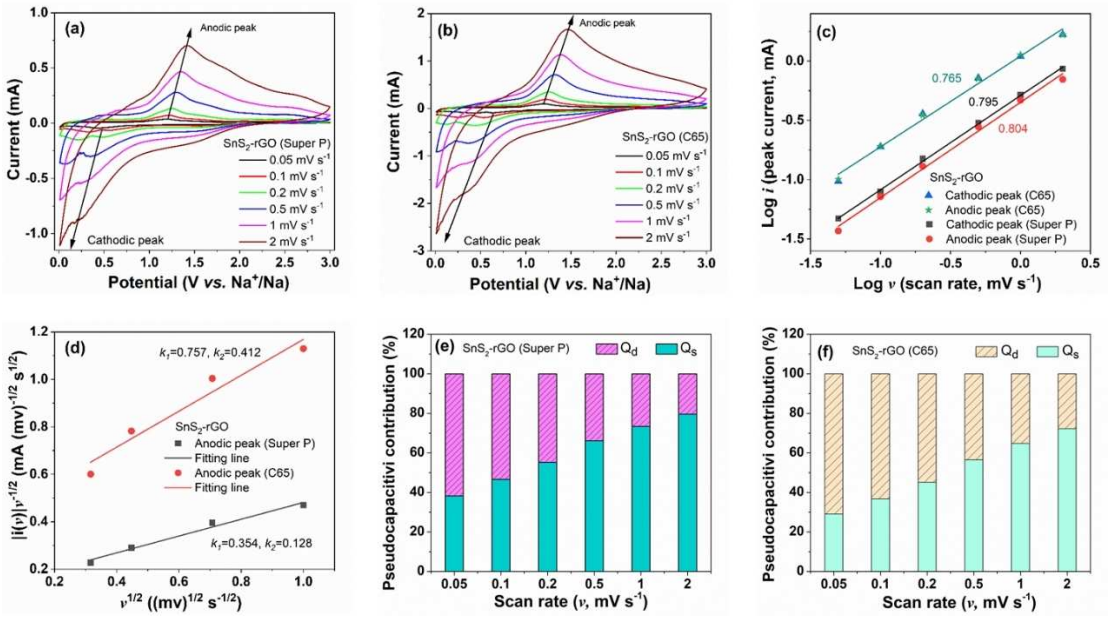

Figure 5. CV curves at various scan rates ranging from 0.05 to 2 mV s^{-1} of SnS_2-rGO with Super P (a) and C65 (b); the relationship of log *i* vs. log *v* plots at each redox peak (c); the linear fitting of $|i(v)|v^{-1/2}$ and $v^{1/2}$ at the selected potentials (d). Bar chart exhibiting the contribution ratio of surface-controlled contribution at different scan rates of SnS_2-rGO with Super P (e) and C65 (f).

To further track the kinetics of sodiation/de-sodiation processes upon cycling, EIS was performed at chosen cycles, as shown in Figure 6. The Nyquist plots of the SnS_2-rGO electrode with Super P at various cycles (1st, 10th, 20th, 30th, and 40th) at the bias potential of 1.05 V vs. Na^+ / Na during sodiation and de-sodiation processes are presented in Figure 6a and b, respectively. Correspondingly, the Nyquist plots of the SnS_2-rGO electrode with C65 are shown in Figure 6c and d. The inset in Figure 6 shows the zoom in the high-frequency area. Each EIS plot contains several semicircles (in the high to medium-frequency region) and a straight line (in the low-frequency region). The small semicircle in the high-frequency region is generally attributed to Na^+ or K^+ mobility through the SEI (R_{SEI}); in the medium frequency region, the semicircle is assigned to the charge transfer (R_{CT}); the straight line in the low-frequency region is related to the Na^+ or K^+ diffusion in the material (*W*).[60] The value of the semicircle's diameter in the middle-frequency region corresponds to the charge-transfer resistance (R_{CT}) of the electrochemical reaction.[61,62] Note that the diameter of the semicircle for SnS_2-rGO with Super P and C65 decreases upon cycling. This R_{CT} decrease could be due to a partial dissolution of the SEI layer. In addition, the slope in the low-frequency region for the SnS_2-rGO electrode with Super P increases upon cycling (Figure 6a and b). The slope of the SnS_2-rGO electrode with C65 also shows the same phenomenon. This implies that the diffusion resistance increases with the cycle number with both carbon additives.

Figure S9 presents resistance values as obtained by fitting the model parameters of the equivalent circuit to match with the observed impedance spectra in sodiation and de-sodiation conditions with Relaxis 3 software. The internal resistance R_i (i = intercept or R internal, contains the resistance of other components like the separator, connector cables etc.) for the SnS_2-rGO with Super P and with C65 are almost unchanged upon cycling (Figure S9a and d). The obtained values of the R_{SEI} are shown in Figure S9b and e. During the sodiation process, the values of R_{SEI} for SnS_2-rGO with Super P and with C65 are sharply decreasing from 450 Ω to around 100 Ω upon cycling. However, the value of R_{SEI} for SnS_2-rGO displays different tendencies in de-sodiation states depending on the respective carbon: R_{SEI} decreases for SnS_2-rGO with Super P from 100 Ω to 40 Ω, but first decreases for SnS_2-rGO with C65 from 60 to 40 Ω followed by a reincrease to the stable value of 80 Ω. This different behavior could be due to the instability of the electrode with Super P leading to the SEI layer cracking and might be the reason for the much lower specific capacity in comparison with electrodes containing the C65 carbon additive. Furthermore, R_{SEI} in sodiation condition is higher than that during desodiation state for both carbon additives, implying the dynamic nature of the SEI layer, which forms during the sodiation process and partially decomposes during desodiation process. As also previously observed for $Zn_2Mn_4O_2$.[63,64] R_{CT} of SnS_2-rGO with Super P and with C65 drastically decrease from 1000 Ω to 400 Ω after the first 10 cycles and remain stable upon cycling (Figure S9c and f). For de-sodiation, the R_{CT} value decreases upon cycling. The R_{CT} increase indicates that the particle size could increase due to active material aggregation during cycling.

To confirm this assumption and track the surface morphology of the SnS_2-rGO electrode upon cycling, SEM was employed. The fresh SnS_2-rGO electrode consists of nanosheets interconnected with conductive carbon, and the active material

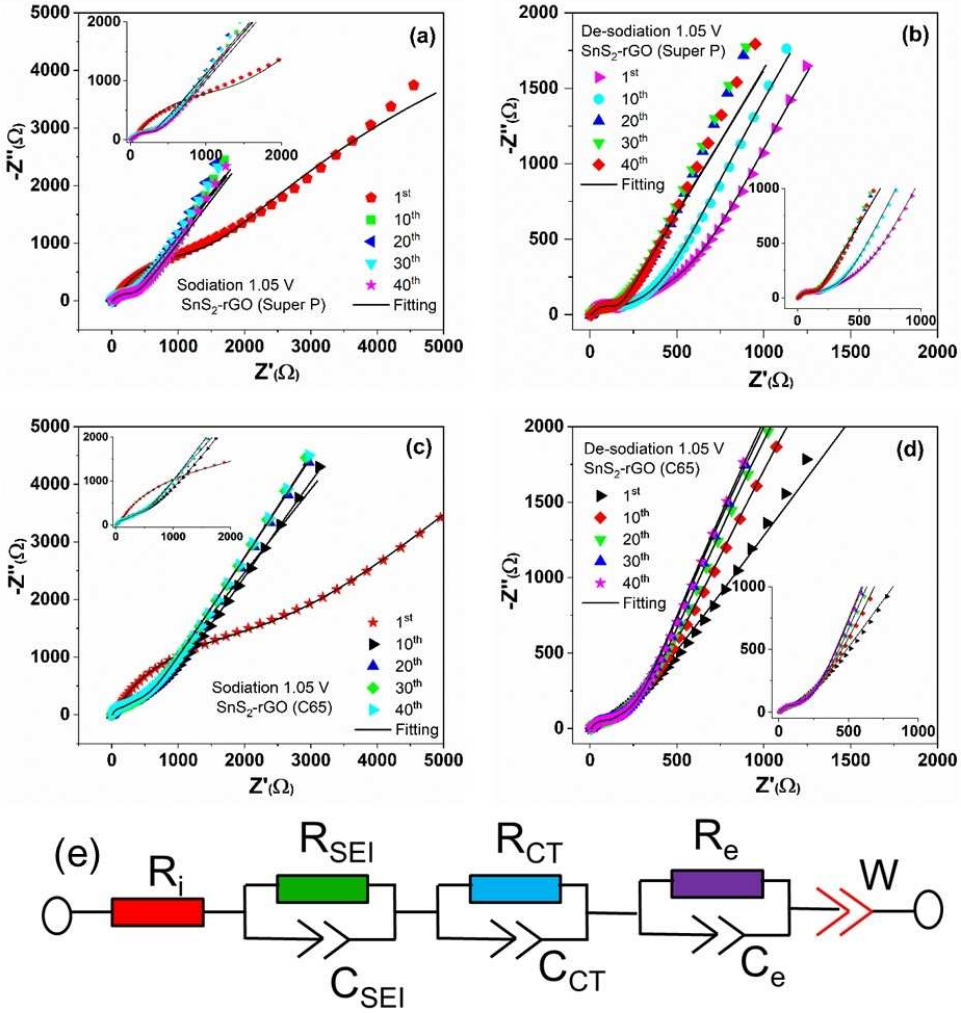

Figure 6. Nyquist plots of the SnS_2-rGO electrode at different cycle numbers in sodiation (a, c) and desodiation (b, d) conditions (1.05 V) with Super P (a, b) and C65 (c, d). The insets display the zoom of Nyquist plots in the high-frequency region. The equivalent circuit is used to fit the EIS experiment data (e).

SnS_2-rGO is surrounded by carbon. As observed from SEM images, the fresh SnS_2-rGO electrode with C65 is more homogeneous than that of Super P (Figure S10a, b). After 20 cycles, the SnS_2-rGO with Super P presents some cracks and is totally covered by the SEI layer, while the SnS_2-rGO with C65 exhibits fewer SEI on the active surface, and some active particles are not covered (Figure S11a, b).

Characterization of K^+ storage performance

The SnS_2-rGO electrode delivers high Na^+ capacities due to both conversion and alloying processes and high-rate performance due to its unique two-dimensional porous layered structure with large interlayer spacing. Therefore, it is worth investigating the SnS_2-rGO towards the insertion of the next alkali ion: potassium. KIBs with abundant potassium resources around the world and a low standard hydrogen potential (close to that of lithium) make KIBs an alternative candidate to replace or complement LIBs in large-scale energy storage applications.

In the above characterization of Na^+ storage performance, FEC was identified as a useful additive in 1 M ($NaClO_4$ in EC/DMC = 1 : 1 by mass) for improving the long-term stability of the SnS_2-rGO/Na half-cell. To further check the applicability of the FEC additive in potassium cells, we investigated the long-term cycling stability of the SnS_2-rGO electrode in 1 M KFSI/ EC: DMC (1 : 1 by mass) with 5 wt% FEC additive and without. Figure 7a and b compare the cyclic stability of the SnS_2-rGO electrode with Super P and C65. The cycling behavior of the cell without FEC additive is superior to the cell with 5 wt% FEC additive for both cases with Super P and with C65 carbon additives. All depotassiation capacities of the SnS_2-rGO electrodes and efficiencies of half-cells decrease when 5 wt% FEC are added with Super P and C65. These results demonstrate that the function of electrolyte additives is not generally valid for all alkali-metal ion cells, but needs to be checked for each cell concept individually. Bie et al.[34] also reported that the FEC additive has a disadvantageous influence on the cycling stability of graphitic negatives in 0.7 M KPF_6 in EC/DEC (1 : 1 *v*/*v*) for potassium cells. It could be concluded that the role of the

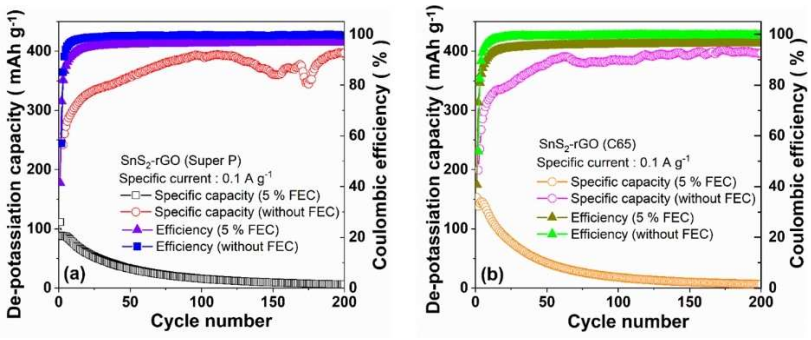

Figure 7. (a) Comparison of the SnS_2-rGO electrode in 5 wt% FEC-containing and FEC-free electrolyte with Super P (a) and C65 conductive additive (b).

FEC additive is different in sodium and potassium cells. Therefore, 1 M KFSI in EC/DMC (1:1 by mass) electrolyte without FEC additive was used in the following electrochemical measurements in this work.

Figure S12 shows SEM images of the SnS_2-rGO electrode in the FEC-free electrolyte (Figure S12a, b) and 5 wt% FEC-containing electrolytes (Figure S12c, d) after 20 cycles. A smooth and thin SEI film covers the SnS_2-rGO electrode when it is cycled with the FEC-free electrolyte. However, some nanospheres are attached to the SnS_2-rGO electrode when it is cycled with 5 wt% FEC-containing electrolyte. It can be concluded that the FEC electrolyte additive is detrimental and inhibits the formation of a stable SEI in KIBs. The EDS elemental mapping of the SnS_2-rGO electrode with Super P in the FEC-free and 5 wt% FEC-containing electrolytes are presented in Figure S13a and b, respectively. The images show uniform distributions of Sn, S, C, and K, in the discharged product and a homogenous distribution of Sn and S in the charged product. Therefore, it is expected that the peculiar composite structure of SnS_2-rGO keeps its elemental composition during the electrochemical processes. There is no evidence of the formation of regions, which consist solely of carbon or the Sn-based phases.

Potassium-ion storage mechanism and electrochemical performance

Figure 8a and b display the corresponding CV curves at a scan rate of 0.05 mV s^{-1} in a voltage range from 0.01 to 3.0 V vs. K^+/K, respectively. According to previous reports,[18,65–67] in the first cathodic scan, the small peak located at 2.40 V can be assigned to the K^+-ion insertion into the SnS_2 material [Eq. (8)]. The peaks

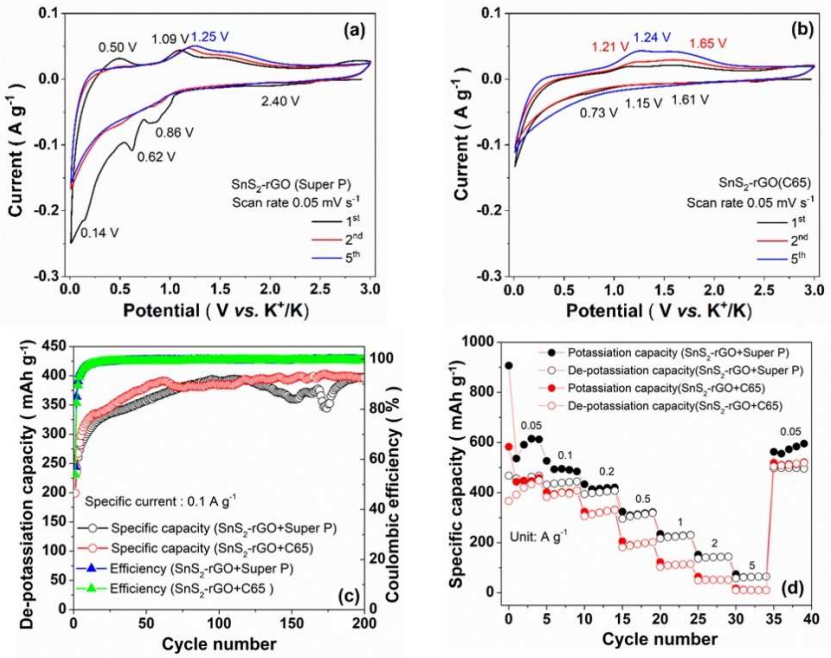

Figure 8. CV curves of the SnS_2-rGO electrode at a scan rate of 0.05 mV s^{-1} in the voltage range from 0.01 to 3.0 V vs. K^+/K with Super P (a) and C65 (b), respectively. Electrochemical performances of SnS_2-rGO electrode: long-term cycling and Coulombic efficiency with Super P and C65 conductivity at the specific current of 0.1 A g^{-1} (c); rate performance with Super P and C65 additives (d).

at 0.86 and 0.62 V for the SnS_2-rGO electrode with Super P and at 0.73 V for that with C65 are assigned to the conversion of SnS into metallic Sn and K_2S and the formation of an SEI film [Eq. (9)]. The peak that emerged at 0.14 V is attributed to an alloying reaction [Eqs. (10) and (11)]. It is observed that the reduction peaks (0.86, 0.62, and 0.73 V) become weaker in the subsequent scan, correspondingly, in the first anodic scan, the oxidation peak at 0.50 V is related to the de-alloying of KSn, and the peak at 1.05 V to the formation of K_xSnS_2. The distinct oxidation peak at 1.61 V is related to the restitution of the original SnS_2-rGO. Additionally, the CV curves are very similar for the 2nd and 3rd cycles, implying good electrochemical reversibility of the SnS_2-rGO composite upon potassiation and depotassiation reactions. It's observed that the SnS_2-rGO electrode with Super P has more redox peaks than that with C65 carbon additive, and the CV area with Super P is larger than that with C65. This indicates that Super P conductive carbon enables an increased rate of electrochemical reactions, therefore, higher K-ion storage ability, which will be discussed later.

$$SnS_2 + 2K^+ + 2e^- \rightleftharpoons SnS + K_2S \quad (8)$$

$$SnS + 2K^+ + 2e^- \rightleftharpoons Sn + K_2S \quad (9)$$

$$23Sn + 4K^+ + 4e^- \rightleftharpoons K_4Sn_{23} \quad (10)$$

$$K_4Sn_{23} + 19K^+ + 19e^- \rightleftharpoons 23KSn \quad (11)$$

Figure 8c shows the long-term cycling performance of the SnS_2-rGO electrode with Super P and C65 at the specific current of 0.1 $A\,g^{-1}$ within the potential range from 0.01 to 3.0 V vs. K^+/K. Both electrodes display specific capacity increases upon cycling. The specific capacity of the SnS_2-rGO electrode with Super P increases from 247 to 398 $mAh\,g^{-1}$ from the 1st to 200th cycle. Similarly, the specific capacity of the SnS_2-rGO electrode with C65 increases from 199 to 398 $mAh\,g^{-1}$. Formation and activation processes are well-known and always applied to commercial batteries after production. The initial capacity increase is not unusual, for example, during the SEI formation. Two reasons are possible for the increase of depotassiation capacities of the SnS_2-rGO electrode during the first 50 cycles: 1) activation process: the SnS_2-rGO electrode activation process continues for many more cycles with a gradual capacity increase. Yang et al.[68] reported anatase TiO_2 nanocubes showed excellent rate capability and cycling stability after a gradual activation process. A similar electrochemical activation phenomenon for Co_3O_4 hollow spheres as lithium-ion anodes has been reported.[69] 2) Pulverized SnS_2 nanoparticles are distributed on rGO substrate after the initial cycles: these pulverized SnS_2 particles exhibit pseudo-capacitive behavior, which is accompanied by the simultaneous capacity increase. The particles transform into smaller ones and tend to interconnect with each other upon cycling. These smaller particles are equally distributed with the interconnected carbon balls, which can enlarge the contact between the SnS_2 nanoparticles and electrolyte, thus resulting in the high efficiency of the electrochemical reaction, which is the second probable reason for the capacity increase in the first 50 cycles. The SnS_2-rGO electrodes with Super P and C65 both reach high Coulombic efficiencies (99.8%) except for the first few cycles. However, the capacity of pure SnS_2 electrode displays 282 $mAh\,g^{-1}$ at 0.1 $A\,g^{-1}$.[70] The pure rGO electrode presents 78 $mAh\,g^{-1}$ at the same current. Therefore the SnS_2-rGO electrode shows enhance cycling performance.

Figure 8d depicts the rate performance of the SnS_2-rGO electrode at various specific currents from 0.05 to 5 $A\,g^{-1}$ in the voltage range between 0.01 and 3.0 V vs. K^+/K. The rate performance of the SnS_2-rGO with Super P electrode is better than that of the C65-based electrode. At the first low current density of 0.05 $A\,g^{-1}$, the SnS_2-rGO electrode with Super P presents a high reversible capacity of 446 $mAh\,g^{-1}$. By increasing the specific currents to 0.1, 0.2, 0.5, 1, 2, and 5 $A\,g^{-1}$, the specific capacity decreases to 439, 402, 310, 225, 142, and 63 $mAh\,g^{-1}$, respectively. When the specific current returns to 0.05 $A\,g^{-1}$, the cell delivers 499 $mAh\,g^{-1}$, which is even a higher value than the initial capacity of 446 $mAh\,g^{-1}$. In contrast, the specific capacity of the SnS_2-rGO electrode with C65 is much lower than that of the Super P-based electrode tested under the same specific currents. The specific capacity of the SnS_2-rGO electrode with C65 delivers 420, 400, 320, 194, 112, 52, and 11 $mAh\,g^{-1}$ at specific currents of 0.05, 0.1, 0.2, 0.5, 1, 2, and 5 $A\,g^{-1}$, respectively.

Figure S14a and b present the potassiation/depotassiation voltage profiles of the SnS_2-rGO electrodes with Super P and C65 at the 1st, 2nd, 50th, 100th, and 200th cycle at a specific current of 0.1 $A\,g^{-1}$. In agreement with the CV curves, the plateaus and slopes appear in the first potassiation process, which are attributed to the formation of K_xSnS_2 (2.40 V), the conversion reaction (0.83–0.70 V), and alloying reaction (0.01–0.60 V), respectively. Moreover, the first de-potassiation potential plateau at 0.50 V is due to the de-alloying reaction. The pronounced plateau located at 1.09 V is assigned to K^+-ion extraction from the previously potassiated material. The SnS_2-rGO electrode with Super P delivers a first potassiation capacity of 433 $mAh\,g^{-1}$ and a depotassiation capacity of 247 $mAh\,g^{-1}$ with a CE of 57.0%. The irreversible capacity of 186 $mAh\,g^{-1}$ at the first cycle is due to the inevitable electrolyte decomposition and consequent formation of the SEI layer on the surface of the active material.[52] In the following cycles, the SnS_2-rGO electrode with Super P shows an increase in the de-potassiation capacity. The depotassiation capacity has a value of 398 $mAh\,g^{-1}$ at the 200th cycle. In comparison, the SnS_2-rGO electrode with C65 presents a first potassiation capacity of 369 $mAh\,g^{-1}$ and a depotassiation capacity of 199 $mAh\,g^{-1}$ with a CE of 54.0%. With C65, the irreversible capacity of the first cycle is 170 $mAh\,g^{-1}$. The CE increases to 99% at the second cycle and is stable in the subsequent cycles, implying the high reversibility of the electrochemical reactions. The depotassiation capacity of the Super P-containing electrode shows fluctuations between the 120th to 170th cycle, while the C65-based electrode displays a more stable depotassiation capacity. This result could be attributed to the higher K-ion storage ability of Super P, leading to electrode cracking (Figure S15). Figure S14c and d compare the specific capacity values of the SnS_2-rGO

electrode with Super P and C65 at the various specific currents, respectively. Note that the rate performance of the electrode with C65 in KIBs is worse than in NIBs, which could be due to the different interactions of K^+ and Na^+ ions with the conductive carbons than of the Na^+ ions. Summary of the Sn-based sulfides electrodes materials for KIBs applications is shown in Table S3.

The influence of the surface-controlled behavior is investigated to understand the differences in rate capability of the SnS_2-rGO electrodes. Figure 9a and b show CV curves of the SnS_2-rGO electrode with Super P and C65 at different scan rates ranging from 0.05 to 2 mV s^{-1}, respectively. As presented in Figure 9c, the *b* value can be determined from the linear fitting of the log (*i*) vs. log (*v*) curve [Eqs. (4) and (5)].[56–58] The value of *b* for the SnS_2-rGO electrode with Super P is 0.645 for the anodic peaks. In the case of the SnS_2-rGO electrode with C65, the *b* value for the anodic peaks is 0.720, which indicates that the electrochemical behavior of the SnS_2-rGO electrode is composed of both diffusion processes and surface-controlled processes. According to Brezesinski et al.[56] a quantitative analysis was conducted to determine the fraction of surface-controlled reaction in the CV curve [Eqs. (6) and (7)]. Figure 9d displays the relationship of $|i(v)|v^{-1/2}$ and $v^{1/2}$, and the related of coefficients k_1 and k_2. For the SnS_2-rGO electrode with Super P (Figure 9e), the percentage of the surface-controlled process increases from 15.0, 20.0, 26.1, 35.9, 44.2, to 52.8% with a scan rate increase of 0.05, 0.1, 0.2, 0.5, 1, and 2 mV s^{-1},[1]. Similarly, the proportion of the surface-controlled processes for the SnS_2-rGO electrode with C65 (Figure 9f) increases from 19.9, 26.0, 33.2, 44.0, 52.6, to 61.1%, which indicates that surface-controlled behavior holds competitive advantages in the whole electrochemical process especially at high scan rates. From Figure S16a and b, it can be seen that the surface-controlled contribution (Q_p) is 35.9% and 44.0% of the total charge storage at a scan rate of 0.5 mV s^{-1} for SnS_2-rGO with Super P and C65, respectively.

To further investigate the kinetics of potassiation/de-potassiation processes upon cycling, EIS was performed at different cycles, and the Nyquist plots are shown in Figure 10. The Nyquist plots of the SnS_2-rGO electrode with Super P and with C65 at various cycles (1st, 10th, 20th, 30th, and 40th) at the fixed potential of 0.48 V vs. K^+/K during potassiation/de-potassiation processes are presented in Figure 10a and b, and c and d, respectively.[61,62] It is observed that the diameter of the semicircle for SnS_2-rGO with Super P and C65 increases upon cycling. The R_{CT} value increases could be due to active polarization and electrolyte decomposition. Additionally, the slope in the low-frequency region for the SnS_2-rGO with Super P and with C65, decreases upon cycling, which implies that the diffusion resistance decreases with cycling.

The electronic resistance R_e of the SnS_2-rGO with Super P electrode is lower than that of C65 carbon additive (Figure S17a and d). The R_{SEI} value of the SnS_2-rGO with Super P increases from 5767 to 6623 Ω during the potassiation process and from 3435 to 5401 Ω during the de-potassiation process upon cycling. In contrast, the R_{SEI} value of the SnS_2-rGO with C65 decreases from 2654 to 1300 Ω during the potassiation process and from 1800 to 900 Ω during the de-potassiation process upon cycling (Figure S18b and e). This could be due to a different form of the SEI layer. The homogeneity and thickness of the SEI can be affected when changing conductive carbon. Pfeifer et al.[71] systematic studied six different carbon materials (different carbon morphologies, sizes, amounts of impurities, graphitization, surface areas, pore volumes) on Sb/C electrodes

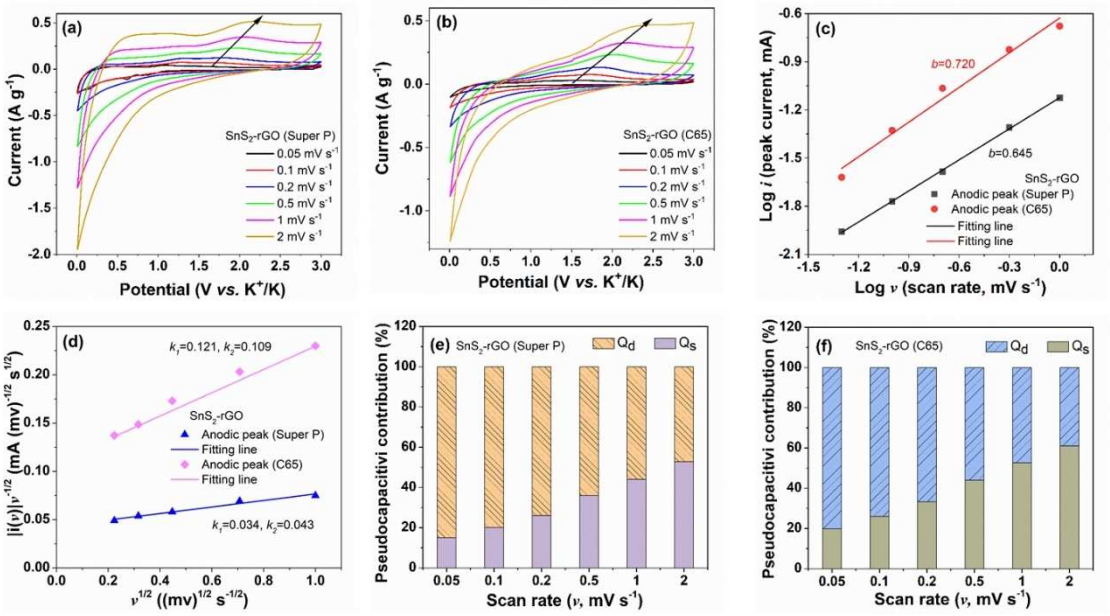

Figure 9. CV curves at different scan rates ranging from 0.05 to 2 mV s^{-1} of SnS_2-rGO with Super P (a) and C65 (b); the linear fitting of log *i* vs. log *v* plots at each redox peak (c); the relationship of linear fitting of $|i(v)|v^{-1/2}$ and $v^{1/2}$ at the selected potentials (d). Bar chart exhibiting the contribution ratio of surface-controlled contribution at different scan rates of SnS_2-rGO with Super P (e) and C65 (f).

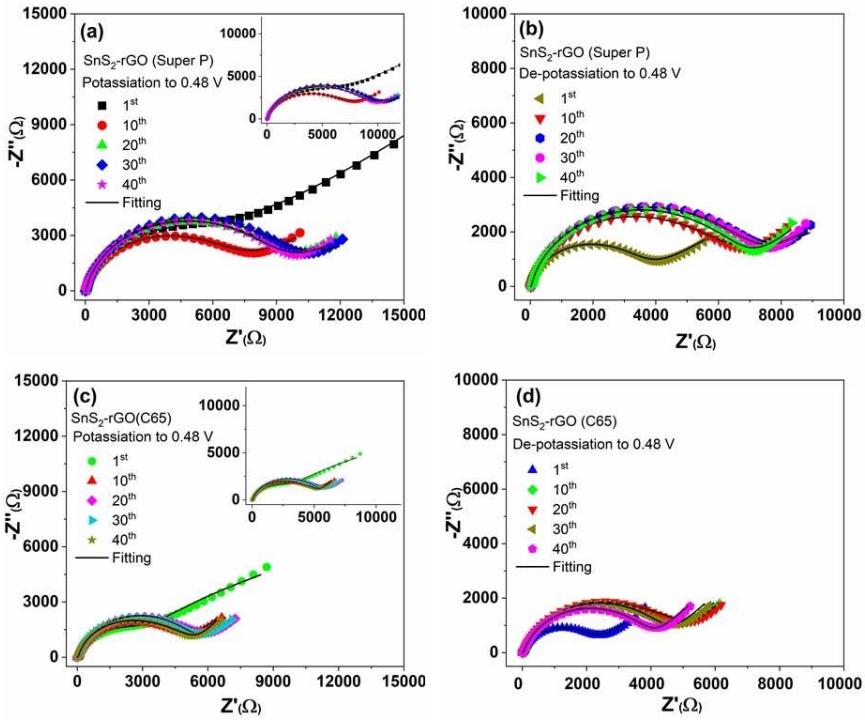

Figure 10. Nyquist plots of the SnS_2-rGO electrode with Super P at different cycles in potassiation (a) and depotassiation (b) states (0.48 V); Nyquist plots of the SnS_2-rGO electrode with C65 at various cycles in in potassiation (c) and depotassiation (d) conditions (0.48 V).

in NIBs. They identified the critical aspects, which are beneficial and improve the electrochemistry of Sb/C electrodes. Most probably, Super P forms a more homogenous and thicker SEI layer which can protect the active material and lead to a superior rate capability. Furthermore, the changes of R_{CT} with cycling are investigated (Figure S17c and f). The SEI and electrode cracking upon cycling could be the reason for the R_{CT} increases in the case of the SnS_2-rGO with C65. The big differences in the R_{CT} resistance values depending on the different carbon additives (Super P and C65) lead to different cycling performances and especially different rate performances.

Fewer cracks and smoother surfaces are observed on the SnS_2-rGO electrode with Super P in Figure S18a, while more cracks and active materials expansion can be observed on the SnS_2-rGO electrode with C65 in Figure S18b. Therefore, the Super P additive results in superior cycling stability than C65 due to the more stable SEI film and better contact between active particles.

Conclusion

In summary, porous few-layer SnS_2 nanosheets have been grown in situ on reduced graphene oxide to form an SnS_2-rGO sandwich structure via a strong C–O–Sn bond. This peculiar structure not only ensures rapid Na-ion/K-ion diffusion and efficient electron transport throughout bulk material, but also provides a good structure stability to buffer the large volume change during repeated cycling processes. Owing to the designed nanoarchitecture, the SnS_2-rGO negative electrode delivers high reversible desodiation capacities (635 mAh g^{-1} at 0.2 A g^{-1} after 250 cycles) and depotassiation capacities (398 mAh g^{-1} at 0.1 A g^{-1} after 200 cycles). Moreover, this work demonstrated that the electrolyte additive (FEC) can improve the specific capacity and stability of the SnS_2-rGO electrode in Na half-cells, while negatively affecting the performance in K half-cells. The impact of two carbon additives on the performance of the SnS_2-rGO material is evaluated both in Na and K half-cells.

It is found that the SnS_2-rGO electrode with C65 has superior long-term cycling and rate performance when compared to the electrodes with Super P in NIBs. This is most probably due to the charge storage capability of Super P, which is electrochemically active. This electrochemical activity could detrimentally impact the active material, leading to a loss of buffering features and causing the SnS_2-rGO electrode cracking. The increase in R_{SEI} values as calculated from the electrochemical impedance spectra agrees with the possible cracking and contact loss of the SnS_2-rGO- Super P electrode. If Super P itself expands, the conductive path can be interrupted, thus leading to a capacity loss upon long cycling. In contrast, the SnS_2-rGO electrode with Super P shows a better rate performance than that with C65 in KIBs, which could be due to the insertion of K^+ ions into the conductive carbon. This insertion behavior for K^+-ions is different from Na^+ ions. Most probably, the insertion mechanism in KIBs has less impact on the performance than that in NIBs. This effect should be further

investigated, focusing on the insertion mechanism of Na^+ and K^+ in Super P and the subsequent characteristics of Super P. This finding will not only be helpful for a more complete understanding of the reaction mechanism of Sn-based sulfides negative materials but also will offer valuable guidance for developing new negative materials with higher capacities for the next generation rechargeable batteries "beyond lithium".

Experimental Section

Synthesis $MnCO_3$ microcubes template

$MnCO_3$ microcubes were synthesized by a simple mixing method.[72] Typically, $MnSO_4{\cdot}H_2O$ (1 mmol) and $(NH_4)_2SO_4$ (10 mmol) were dissolved in water (70 mL) and ethanol (7 mL) solvents with stirring. NH_4HCO_3 (10 mmol) was dissolved in water (70 mL) with stirring. After all solutions had complete dispersion, the NH_4HCO_3 solution was added to the mixture mentioned above at room temperature. After around 2 min the final solution turned milky white, which indicated the initial formation of $MnCO_3$ microcubes. The mixture solution was maintained at 50 °C and aged for 9 h in an oven. $MnCO_3$ microcubes were separated from the reaction mixture by centrifugation and washed several times with deionized water and ethanol to remove impurities. Finally, $MnCO_3$ microcubes were dried at 50 °C in an oven.

Synthesis $MnCO_3$@SnS_2-rGO

210 mg Tin(IV) chloride pentahydrate ($SnCl_4{\cdot}5H_2O$, Sigma–Aldrich, 98%) and 300 mg thioacetamide acid (TAA, C_2H_5NS, Sigma-Aldrich, 99%) were dissolved in 50 mL of ethanol solution. Subsequently, 140 mg as-prepared $MnCO_3$ microcubes template was dispersed in the above solution. Then, 10 mL graphene oxide solution (4 mg mL^{-1}, dispersion in H_2O, Sigma-Aldrich) was added to the mixture solution. The mixture solution was stirred for 60 min at room temperature. Finally, the solution was transferred into a 100 mL Teflon-lined autoclave and heated at 120 °C for 12 h. After cooling down to room temperature, the product was centrifuged and washed serval times with deionized water. The product was dried at 80 °C.

Synthesis porous SnS_2-rGO

The above-harvested $MnCO_3$@SnS_2-rGO (75 mg) was dispersed into the hydrochloric acid solution (0.1 M, 10 mL) to selectively remove the $MnCO_3$ microcubes template at room temperature for 24 h. After washing with deionized water several times, the final product SnS_2-rGO was dried at 60 °C.

Material characterization

The crystal structure and phase purity of the sample was conducted at PETRA-III (DESY, Hamburg) by using the high-resolution powder diffraction beamline P02.1 ($\lambda = 0.207230$ Å). The morphology and elemental distribution of the sample were investigated by scanning electron microscope (SEM, Carl Zeiss SMT AG) coupled with energy-dispersive spectroscopy (EDS, Quantax 400 SDD, Bruker). Raman spectra were measured by Raman spectrometer (LabRam Evolution HR, HORIBA Jobin Yvon) at $\lambda = 532$ nm. Scanning transmission electron microscopy (STEM) and high-resolution transmission electron microscopy (HR-TEM) of the samples were carried out on an aberration (image) corrected transmission electron microscope (FEI Company, Titan 80-300) via a Gatan US1000 slow-scan CCD camera. X-ray photoelectron spectroscopy (XPS) measurements were performed using a K-Alpha$^+$ XPS spectrometer (Thermo-Fisher Scientific, East Grinstead, U.K.). Thermogravimetric analysis (TGA, NETZSCH TG 209F1 Libra) was carried out to confirm the carbon content in composites. Thermo Avantage software was applied in data acquisition and processing, as described elsewhere by Parry et al.[73] All samples were examined using a micro-focused, monochromated $Al_{K\alpha}$ X-ray source (400 mm spot size). The spectra are referenced in binding energy to the C1 s peak (C–C, C–H) at 285.0 eV binding energy.[74]

Electrochemical characterization

The working electrode was fabricated by mixing 70 mass% SnS_2-rGO powder, 20 mass% carbon black (C65, Timcal Ltd.), and 10 mass% carboxymethyl cellulose (Sigma–Aldrich) dissolved in deionized water (3 wt%) in a speed-mixer (DAC150.1 FVZ) from Hauschild. SnS_2-rGO and carbon black were first mixed at 800 rpm for 2 min without solvent. Then, ethanol was added and mixed (1000 rpm for 10 min and 2500 rpm for 10 min, respectively) to harvest a viscous paste. Finally, the binder solution was added and mixed at 800 rpm for 10 min. the slurry was coated on aluminum foil and dried at 80 °C for one day. Then, the electrodes were cut into discs (12 mm in diameter) and dried at 120 °C overnight under vacuum. The mass loading of SnS_2-rGO is 1.0 ± 0.01 mg cm^{-2} with a thickness of 65 μm. For comparison, another carbon conductivity (Super P, Timcal Ltd.) was used, and the working electrode was made in the same way.

Electrochemical measurements were performed by using three-electrode Swagelok-type half-cells, the cells were assembled inside an argon-filled glovebox (MBraun, O_2 and $H_2O \leq 0.01$ ppm). For NIBs cells, a sodium metal foil as a counter electrode and reference electrode. 1 M sodium perchlorate ($NaClO_4$) dissolved into ethylene carbonate/dimethyl carbonate (EC/DMC = 1 : 1 in mass) was used as sodium-based electrolyte. For KIBs cells, a potassium metal foil was used as a counter electrode and reference electrode. 1 M potassium bis(fluorosulfonyl)imide (KFSI) dissolved into EC/DMC = 1 : 1 in mass was used as potassium-based electrolyte. A glass-fiber disc (Whatman GF/D) was used as a separator. 5 wt% fluoroethylene carbonate (FEC) as electrolyte additive was added into $NaClO_4$ and KFSI electrolytes, respectively. All electrochemical measurements were conducted on multichannel potentiostat (VMP3, Bio-Logic), and the cells were put in a climate chamber (binder) at room temperature. Galvanostatic discharge/charge curves with potential limitation (GCPL) and cyclic voltammetry (CV) were measured in the potential range of 0.01–3.0 V vs. Na^+/Na and 0.01–3.0 V vs. K^+/K, respectively. Electrochemical impedance spectroscopy (EIS) experiments scanning from 10 mHz to 500 kHz at different selected potentials. The EIS data were collected every 10 cycles and impedance spectra were analyzed utilizing Relaxis 3 software (rhd Instruments, Germany).

Supporting Information

The Supporting Information is available free of charge at https://doi.org/10.1002/cssc.202202281: The EDS elemental maps of the SnS_2-rGO; SEM images, TEM images, Raman and OEA of the SnS_2-rGO; the Nyquist plots of the SnS_2-rGO at some selected cycles (1st, 20th etc) under sodiation/desodiation and potassiation/depotassiation conditions are shown in the Supporting Information.

Acknowledgements

C. Li appreciates financial support from the China Scholarship Council (CSC, Nr: 201707030004) during his PhD study at KIT. The authors also acknowledge DESY (Hamburg, Germany) for providing experimental facilities. The authors would like to acknowledge the financial support by Yunnan Major Scientific and Technological Projects (grant NO.202202AG050003) and Yunnan Fundamental Research Projects (grant NO. 202201BE070001-019). This work contributes to the research performed at CELEST (Center for Electrochemical Energy Storage Ulm-Karlsruhe) and was funded by the German Research Foundation (DFG) under Project ID 390874152 (POLiS Cluster of Excellence, EXC 2154) Open Access funding enabled and organized by Projekt DEAL.

Conflict of Interest

The authors declare no competing financial interest.

Data Availability Statement

The data that support the findings of this study are available from the corresponding author upon reasonable request.

Keywords: fluoroethylene carbonate · sandwich structure · sodium · batteries · potassium

[1] L. Zhang, W. (Alex) Wang, S. Lu, Y. Xiang, *Adv. Energy Mater.* **2021**, *11*, 2003640.
[2] S. Liu, L. Kang, S. C. Jun, *Adv. Mater.* **2021**, *33*, 2004689.
[3] N. Li, M. Sun, W. H. Kan, Z. Zhuo, S. Hwang, S. E. Renfrew, M. Avdeev, A. Huq, B. D. McCloskey, D. Su, W. Yang, W. Tong, *Nat. Commun.* **2021**, *12*, 2348.
[4] M. Zhou, P. Bai, X. Ji, J. Yang, C. Wang, Y. Xu, *Adv. Mater.* **2021**, *33*, 2003741.
[5] W. Zhou, M. Zhang, X. Kong, W. Huang, Q. Zhang, *Adv. Sci.* **2021**, *8*, 2004490.
[6] D. Adekoya, S. Qian, X. Gu, W. Wen, D. Li, J. Ma, S. Zhang, *Nano-Micro Lett.* **2021**, *13*, 13.
[7] R. Guo, L. Li, B. Wang, Y. Xiang, G. Zou, Y. Zhu, H. Hou, X. Ji, *Energy Storage Mater.* **2021**, *37*, 8–39.
[8] J. Sung, N. Kim, J. Ma, J. H. Lee, S. H. Joo, T. Lee, S. Chae, M. Yoon, Y. Lee, J. Hwang, S. K. Kwak, J. Cho, *Nat. Energy* **2021**, *6*, 1164–1175.
[9] J. Sun, H.-W. Lee, M. Pasta, H. Yuan, G. Zheng, Y. Sun, Y. Li, Y. Cui, *Nat. Nanotechnol.* **2015**, *10*, 980–985.
[10] J. Han, M. Xu, Y. Niu, G.-N. Li, M. Wang, Y. Zhang, M. Jia, C. M. Li, *Chem. Commun.* **2016**, *52*, 11274–11276.
[11] J. Yang, Z. Ju, Y. Jiang, Z. Xing, B. Xi, J. Feng, S. Xiong, *Adv. Mater.* **2018**, *30*, 1700104.
[12] W. Luo, J. Wan, B. Ozdemir, W. Bao, Y. Chen, J. Dai, H. Lin, Y. Xu, F. Gu, V. Barone, L. Hu, *Nano Lett.* **2015**, *15*, 7671–7677.
[13] T. Jin, P. F. Wang, Q. C. Wang, K. Zhu, T. Deng, J. Zhang, W. Zhang, X. Q. Yang, L. Jiao, C. Wang, *Angew. Chem. Int. Ed.* **2020**, *59*, 14511–14516; *Angew. Chem.* **2020**, *132*, 14619–14624.
[14] J. Wang, B. Wang, H. Sun, G. Wang, J. Bai, H. Wang, *Energy Storage Mater.* **2022**, *46*, 394–405.
[15] Z. Jian, W. Luo, X. Ji, *J. Am. Chem. Soc.* **2015**, *137*, 11566–11569.
[16] Z. Jian, Z. Xing, C. Bommier, Z. Li, X. Ji, *Adv. Energy Mater.* **2016**, *6*, 1501874.
[17] D. Li, Q. Sun, Y. Zhang, L. Chen, Z. Wang, Z. Liang, P. Si, L. Ci, *ChemSusChem* **2019**, *12*, 2689–2700.
[18] K. Huang, Z. Xing, L. Wang, X. Wu, W. Zhao, X. Qi, H. Wang, Z. Ju, *J. Mater. Chem. A* **2018**, *6*, 434–442.
[19] R. Rajagopalan, Y. Tang, X. Ji, C. Jia, H. Wang, *Adv. Funct. Mater.* **2020**, *30*, 1909486.
[20] Y. Kim, Y. Kim, A. Choi, S. Woo, D. Mok, N.-S. Choi, Y. S. Jung, J. H. Ryu, S. M. Oh, K. T. Lee, *Adv. Mater.* **2014**, *26*, 4139–4144.
[21] W. Zhang, W. K. Pang, V. Sencadas, Z. Guo, *Joule* **2018**, *2*, 1534–1547.
[22] L. Fan, X. Li, X. Song, N. Hu, D. Xiong, A. Koo, X. Sun, *ACS Appl. Mater. Interfaces* **2018**, *10*, 2637–2648.
[23] V. Lakshmi, Y. Chen, A. A. Mikhaylov, A. G. Medvedev, I. Sultana, M. M. Rahman, O. Lev, P. V. Prikhodchenko, A. M. Glushenkov, *Chem. Commun.* **2017**, *53*, 8272–8275.
[24] Q. Sun, D. Li, L. Dai, Z. Liang, L. Ci, *Small* **2020**, *16*, 2005023.
[25] B. Qu, C. Ma, G. Ji, C. Xu, J. Xu, Y. S. Meng, T. Wang, J. Y. Lee, *Adv. Mater.* **2014**, *26*, 3854–3859.
[26] Y. Ren, J. Wang, X. Huang, J. Ding, *Mater. Lett.* **2017**, *186*, 57–61.
[27] P. Zhou, X. Wang, W. Guan, D. Zhang, L. Fang, Y. Jiang, *ACS Appl. Mater. Interfaces* **2017**, *9*, 6979–6987.
[28] D.-S. Bin, S.-Y. Duan, X.-J. Lin, L. Liu, Y. Liu, Y.-S. Xu, Y.-G. Sun, X.-S. Tao, A.-M. Cao, L.-J. Wan, *Nano Energy* **2019**, *60*, 912–918.
[29] Y. Zhang, C. Zhao, Z. Zeng, J. M. Ang, B. Che, Z. Wang, X. Lu, *Electrochim. Acta* **2018**, *278*, 156–164.
[30] D. Kong, H. He, Q. Song, B. Wang, Q.-H. Yang, L. Zhi, *RSC Adv.* **2014**, *4*, 23372–23376.
[31] M. Sathish, S. Mitani, T. Tomai, I. Honma, *J. Phys. Chem. C* **2012**, *116*, 12475–12481.
[32] Y. Zhang, P. Zhu, L. Huang, J. Xie, S. Zhang, G. Cao, X. Zhao, *Adv. Funct. Mater.* **2015**, *25*, 481–489.
[33] S. Komaba, T. Ishikawa, N. Yabuuchi, W. Murata, A. Ito, Y. Ohsawa, *ACS Appl. Mater. Interfaces* **2011**, *3*, 4165–4168.
[34] X. Bie, K. Kubota, T. Hosaka, K. Chihara, S. Komaba, *J. Mater. Chem. A* **2017**, *5*, 4325–4330.
[35] X. Jiang, X. Yang, Y. Zhu, J. Shen, K. Fan, C. Li, *J. Power Sources* **2013**, *237*, 178–186.
[36] P. Zheng, Z. Dai, Y. Zhang, K. N. Dinh, Y. Zheng, H. Fan, J. Yang, R. Dangol, B. Li, Y. Zong, Q. Yan, X. Liu, *Nanoscale* **2017**, *9*, 14820–14825.
[37] S. Zhang, F. Yao, L. Yang, F. Zhang, S. Xu, *Carbon* **2015**, *93*, 143–150.
[38] Y. Jiang, Y. Feng, B. Xi, S. Kai, K. Mi, J. Feng, J. Zhang, S. Xiong, *J. Mater. Chem. A* **2016**, *4*, 10719–10726.
[39] Z. Wang, Y. Dong, H. Li, Z. Zhao, H. B. Wu, C. Hao, S. Liu, J. Qiu, X. W. Lou, *Nat. Commun.* **2014**, *5*, 5002.
[40] B. Luo, Y. Fang, B. Wang, J. Zhou, H. Song, L. Zhi, *Energy Environ. Sci.* **2012**, *5*, 5226–5230.
[41] C. Chae, H.-J. Noh, J. K. Lee, B. Scrosati, Y.-K. Sun, *Adv. Funct. Mater.* **2014**, *24*, 3036–3042.
[42] Y. Liu, H. Kang, L. Jiao, C. Chen, K. Cao, Y. Wang, H. Yuan, *Nanoscale* **2015**, *7*, 1325–1332.
[43] J. Cui, S. Yao, Z. Lu, J.-Q. Huang, W. G. Chong, F. Ciucci, J.-K. Kim, *Adv. Energy Mater.* **2018**, *8*, 1702488.
[44] Z. Ma, Z. Yao, Y. Cheng, X. Zhang, B. Guo, Y. Lyu, P. Wang, Q. Li, H. Wang, A. Nie, A. Aspuru-Guzik, *Nano Energy* **2020**, *67*, 104276.
[45] K. Pfeifer, M. F. Greenstein, D. Aurbach, X. Luo, H. Ehrenberg, S. Dsoke, *ChemElectroChem* **2020**, *7*, 3487–3495.
[46] K. Pfeifer, S. Arnold, Ö. Budak, X. Luo, V. Presser, H. Ehrenberg, S. Dsoke, *J. Mater. Chem. A* **2020**, *8*, 6092–6104.
[47] J. Wang, C. Luo, J. Mao, Y. Zhu, X. Fan, T. Gao, A. C. Mignerey, C. Wang, *ACS Appl. Mater. Interfaces* **2015**, *7*, 11476–11481.
[48] W. Sun, X. Rui, D. Yang, Z. Sun, B. Li, W. Zhang, Y. Zong, S. Madhavi, S. Dou, Q. Yan, *ACS Nano* **2015**, *9*, 11371–11381.
[49] L. Zeng, L. Zhang, X. Liu, C. Zhang, *Nanomaterials* **2020**, *10*, 1–11.
[50] M. E. Spahr, D. Goers, A. Leone, S. Stallone, E. Grivei, *J. Power Sources* **2011**, *196*, 3404–3413.
[51] M. Widmaier, N. Jäckel, M. Zeiger, M. Abuzarli, C. Engel, L. Bommer, V. Presser, *Electrochim. Acta* **2017**, *247*, 1006–1018.
[52] Z. Zhang, H. Zhao, J. Fang, X. Chang, Z. Li, L. Zhao, *ACS Appl. Mater. Interfaces* **2018**, *10*, 28533–28540.
[53] G. A. Muller, J. B. Cook, H.-S. Kim, S. H. Tolbert, B. Dunn, *Nano Lett.* **2015**, *15*, 1911–1917.
[54] G. Tian, Z. Zhao, A. Sarapulova, C. Das, L. Zhu, S. Liu, A. Missiul, E. Welter, J. Maibach, S. Dsoke, *J. Mater. Chem. A* **2019**, *7*, 15640–15653.
[55] V. Augustyn, J. Come, M. A. Lowe, J. W. Kim, P.-L. Taberna, S. H. Tolbert, H. D. Abruña, P. Simon, B. Dunn, *Nat. Mater.* **2013**, *12*, 518–522.
[56] T. Brezesinski, J. Wang, S. H. Tolbert, B. Dunn, *Nat. Mater.* **2010**, *9*, 146–151.

[57] L. Li, S. Peng, N. Bucher, H.-Y. Chen, N. Shen, A. Nagasubramanian, E. Eldho, S. Hartung, S. Ramakrishna, M. Srinivasan, *Nano Energy* **2017**, *37*, 81–89.
[58] H. Lindström, S. Södergren, A. Solbrand, H. Rensmo, J. Hjelm, A. Hagfeldt, S.-E. Lindquist, *J. Phys. Chem. B* **1997**, *101*, 7717–7722.
[59] C. Li, A. Sarapulova, K. Pfeifer, S. Dsoke, *ChemSusChem* **2020**, *13*, 986–995.
[60] C. Li, A. Sarapulova, Z. Zhao, Q. Fu, V. Trouillet, A. Missiul, E. Welter, S. Dsoke, *Chem. Mater.* **2019**, *31*, 5633–5645.
[61] J.-M. Tarascon, M. Armand, *Nature* **2001**, *414*, 359–367.
[62] J. Huang, Z. Jiang, *Electrochim. Acta* **2008**, *53*, 7756–7759.
[63] S. J. Rezvani, F. Nobili, R. Gunnella, M. Ali, R. Tossici, S. Passerini, A. Di Cicco, *J. Phys. Chem. C* **2017**, *121*, 26379–26388.
[64] S. J. Rezvani, R. Gunnella, A. Witkowska, F. Mueller, M. Pasqualini, F. Nobili, S. Passerini, A. Di Cicco, *ACS Appl. Mater. Interfaces* **2017**, *9*, 4570–4576.
[65] J. Xie, Y. Zhu, N. Zhuang, X. Li, X. Yuan, J. Li, G. Hong, W. Mai, *J. Mater. Chem. A* **2019**, *7*, 19332–19341.
[66] L. Cao, B. Zhang, X. Ou, C. Wang, C. Peng, J. Zhang, *ChemElectroChem* **2019**, *6*, 2254–2263.
[67] C. Sheng, C. Zhang, X. Shen, S. Zhao, L. Fu, Y. Wu, J. Wang, Y. Chen, *Batteries & Supercaps* **2020**, *3*, 56–59.
[68] X. Yang, C. Wang, Y. Yang, Y. Zhang, X. Jia, J. Chen, X. Ji, *J. Mater. Chem. A* **2015**, *3*, 8800–8807.
[69] H. Sun, G. Xin, T. Hu, M. Yu, D. Shao, X. Sun, J. Lian, *Nat. Commun.* **2014**, *5*, 4526.
[70] L. Cao, B. Zhang, X. Ou, C. Wang, C. Peng, J. Zhang, *ChemElectroChem* **2019**, *6*, 2254–2263.
[71] K. Pfeifer, S. Arnold, Ö. Budak, X. Luo, V. Presser, H. Ehrenberg, S. Dsoke, *J. Mater. Chem. A* **2020**, *8*, 6092–6104.
[72] J. B. Fei, Y. Cui, X. H. Yan, W. Qi, Y. Yang, K. W. Wang, Q. He, J. B. Li, *Adv. Mater.* **2008**, *20*, 452–456.
[73] K. L. Parry, A. G. Shard, R. D. Short, R. G. White, J. D. Whittle, A. Wright, *Surf. Interface Anal.* **2006**, *38*, 1497–1504.
[74] Z. Zhao, G. Tian, A. Sarapulova, V. Trouillet, Q. Fu, U. Geckle, H. Ehrenberg, S. Dsoke, *J. Mater. Chem. A* **2018**, *6*, 19381–19392.

Manuscript received: December 8, 2022
Revised manuscript received: December 29, 2022
Accepted manuscript online: January 2, 2023
Version of record online: February 13, 2023